

## Hybrid RANS-LES Simulation of MTU-T161 LPT Profile Forcing LES in the Endwall Boundary Layer by Mesh Refinement

Jakob Voigt\*1, Felix M. Möller<sup>2</sup>, Patrick Bechlars<sup>3</sup>, and Lars Wein<sup>1</sup>

<sup>1</sup>Leibniz University Hannover, Institute of Turbomachinery and Fluid Dynamics, Garbsen, Germany <sup>2</sup>German Aerospace Center (DLR), Institute of Test and Simulation for Gas Turbines, Cologne, Germany <sup>3</sup>MTU Aero Engines AG, Munich, Germany

#### **Abstract**

Seamless hybrid RANS-LES methods provide a practical and cost-effective approach to turbulence modeling, bridging the gap between the precision of Large Eddy Simulations (LES) and the affordability of RANS. These methods employ RANS turbulence models to approximate small-scale turbulence in attached boundary layers, while utilizing LES capabilities to resolve larger eddies in detached flow areas and the turbulent free stream. However, their accuracy in predicting flows in RANS regions is dependent on the model's calibration, which can lead to poor predictions when used beyond their calibration scope. This paper proposes a solution to this limitation by utilizing the grid dependency of the Improved Delayed Detached Eddy Simulations (IDDES) formulation. The aim is to induce LES behavior through grid refinements in key areas, specifically the end-wall boundary layer. The MTU-T161 low-pressure turbine cascade, at a Reynolds number of 90,000, serves as the test case. This study expands upon previous work conducted in the midspan of the turbine by investigating the impact of the approach within end-wall boundary layers. It demonstrates that grid refinements lead to a decrease in the effective hybrid length scale, thereby reducing the influence of the underlying turbulence model. Ultimately, this leads to improved predictions of wake losses in locally refined regions of the flow field. In comparison to uniformly fine grids, this method reduced resource consumption by 45%.

Keywords: Hybrid-RANS-LES, MTU-T161-LPT, grid refinement.

## 1 Introduction

In the application of hybrid RANS-LES methods (referred to as hybrid methods) the intention is to resolve large scales of turbulence in detached regions and in the free stream with LES capabilities, while modeling small-scale, wall-bounded flows with RANS turbulence models. RANS models rely on intensive calibration to derive turbulence information from mean flow quantities. This limits their accuracy to the region of calibration. Unsteady, small-scale and three-dimensional effects are continuously challenging fields when it comes to the prediction accuracy of RANS models. A feasible LES setup resolves approximately 80% of the turbulence spectrum, so that in most cases LES comprise enough information for predicting the flow.

Seamless hybrid methods depend on the grid resolution and on local flow field quantities to decide whether the model behavior is more RANS- or more LES-like. For this reason, the user's choice in spatial discretization is impacting the model and the prediction accuracy. This dependency is used to resolve regions of interest in an LES-style while maintaining low-resolution, low-cost RANS-like simulations in surrounding areas of the computational domain.

In recent studies, Voigt et al. [1] presented this procedure for the prediction of the separation bubble in a quasi-3D set up of the turbine cascade. The test case showed a successfully influenced model behavior, so that it resembled pure LES mode. The investigations focused on the alteration of the models' functions through the local mesh refinement for flow solvers

\*Corresponding author: voigt@tfd.uni-hannover.de

that can handle structured grids only. The method ultimately reduced the modeled turbulent kinetic energy and increased resolved fluctuations. The authors concluded that the local refinements created a gray area problem at the interface from coarse to finer grids. This phenomenon is characterized by relatively small contents of resolved stresses downstream of the refining interface as fluctuations needs a specific flow path to develop.

Similar local mesh refinement studies have been carried out by Kořínek et al. [2] and ElCheikh and ElKhoury [3] about the heat transfer of impinging jet flows and on the flow around urban-like obstacles, respectively. Both found out, that the hybrid methods tend to improve the prediction accuracy with increasing grid resolution.

## 2 Test case

This study focuses on the MTU-T161 low-pressure turbine cascade which was experimentally investigated by Entlesberger et al. [4]. The test case has an exit Reynolds number of 90,000, an isentropic exit Mach number of 0.6 and an inlet turbulent intensity of 4%. At that operating point the profile has a laminar separation bubble on the suction side and end-wall vortices are reaching into the freestream at the blade. This test case was extensively analyzed numerically: Müller-Schindewolffs et al. [5] performed direct numerical simulations (DNS) on a quasi-3D domain to identify RANS modeling deficits in the flow field prediction. Fard Afshar et al. [6] investigated the turbulence anisotropy in the separation region of the blade by means of LES. The authors showed that

the state of turbulence on the suction side of the blade undergoes one- and two-component turbulence before fully developing isotropic behavior at the trailing edge. Morsbach et al. [7] performed LES with a higher order numerical method and focused on the reproduction of boundary conditions such as appropriate, turbulent inflow boundary layers and freestream turbulence for the consistency between RANS and LES computations. Rosenzweig et al. [8] presented a detailed comparison between high fidelity LES and RANS computations. Furthermore, they investigated the influence of boundary layer variations at the inflow. Rosenzweig et al. [9] built up on that by presenting a parameter study of incoming wakes and the unsteady loss mechanisms associated.

## 3 Methodology

In this study, different numerical approaches for the prediction of the flow around the turbine cascade will be compared against each other. The focus lies on the behavior of hybrid methods in the presence of non-homogeneous grid refinements. Details about the grid refinement are given below in the subsection 3.1. Additionally, the numerical studies are carried out on a homogeneous grid of low resolution by the means of RANS and hybrid methods, as well as on a grid of higher resolution with RANS, hybrid methods and (underresolved) LES. The modeling and numerical details are addressed in subsection 3.2.

#### 3.1 Computational Grids

The computational domain is shown in Fig. 1 a). The inlet is located  $2 l_{ax}$  upstream of the blade's leading edge. The outlet is located  $1 l_{ax}$  downstream of the trailing edge. The domain has diverging end-walls. At the inlet, the spanwise extent of the computational domain is  $h(x) = 2.66 l_{ax}$  and at the outlet  $h(x) = 3.7 l_{ax}$ . A coarse mesh is designed in a (U)RANS fashion. At the end-wall and at the blade we realized  $y^+ < 1$ , evaluated with the local magnitude of the wall shear stress and the cell size in wall normal grid direction. A second, finer grid has been designed with the intention to increase the grid resolution in span-wise, pitch-wise and axial direction, while maintaining the wall-normal grid resolution. This was found to be critical for realizing a relative large time-step, as the high-aspect ratio cells close to the wall typically lead to high values in the CFL number. For this reason, the simple approach of splitting of a coarse grid's cells was avoided.

A hybrid, so called *locally refined* grid is assembled from parts of the aforementioned coarse and fine grid. The meridional view onto this mesh is shown in Fig. 1 a). The refinement region is approximately normal to the end-wall and has a proportion of 35% of the flow channel. In the locally refined area, the resolution equals the fine mesh and in the rest of the domain it equals the coarse grid. A further evaluation of the grid design with respect to viscous wall coordinates, the RANS integral length scale criterion, and the resolution of turbulent scales is given in section 4.1.

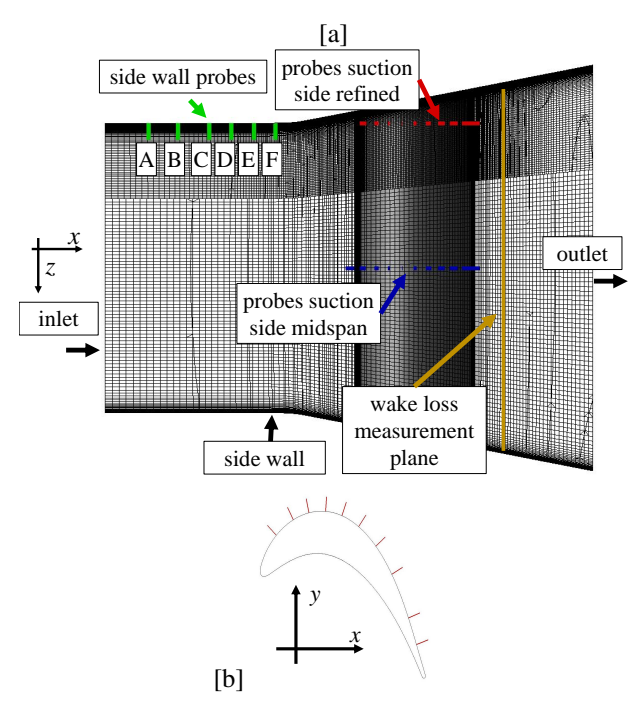


Figure 1: a) Computational domain in meridional view, b) blade surface and probe positions of wall normal probes. The geometries are distorted.

#### 3.2 Modeling Details

All simulations have been conducted using the TRACE<sup>1</sup> solver, which is being developed by the German Aerospace Center (DLR) in cooperation with MTU Aero Engines AG [10]. The governing equations are discretized using second order methods using the Riemann solver according to Roe [11] with central differences for the viscous fluxes. For the RANS methods, the Monotonic Upstream-centered Scheme for Conservation Laws (MUSCL) [12] is used to discretize the convective fluxes. In the case of hybrid methods, a dynamic blending scheme for discretization of the convective fluxes proposed by Travin et al. [13] is employed. This blending scheme switches dynamically between central differencing for accuracy in LES regions and upwind differencing for stability in RANS regions. The IDDES constant au has been set to the convective time unit  $\tau = t_c$ . The latter is calculated as  $t_c = l_{ax}/c_{2,ax} = 3.5 \cdot 10^{-4}$ , with  $l_{ax}$  and  $c_{2,ax}$  being the axial blade length and the axial component of the flux averaged outlet velocity, respectively. For the LES, a constant blending factor of 0.01 was chosen, which leads to 99% central differencing schemes for high accuracy.

In all turbulence resolving simulations, an explicit Runge-Kutta method of third-order of accuracy was used for time integration. Consequently, the CFL number must be less than unity to maintain numerical stability. For the different mesh resolutions and turbulence models this leads to a different time-step size. The time-step sizes utilized are shown in Tab. 1.

LES turbulence modeling is performed with the WALE subgrid scale model [14]. The RANS model used is the Menter

<sup>1</sup>www.trace-portal.de/userguide/

Table 1: Details about the numerical	orids	time discretization and a	veraging times fo	r each numerical method
Table 1. Details about the numerical	grius	, tillic discretization and a	iveraging unics to	i cacii ilulliciicai iliculou

modeling method		LES		
grid name	coarse	locally refined	fine	fine
number of grid cells in 10 <sup>6</sup>	1.9	8.6	20.6	
time-step size in $10^{-8}$ s	3.33	1.67	2.00	
number of time-steps averaged in $10^3$	351	701	584	
time span averaged in $t/t_c$	15	15	1	5

SST model [15] with the production term limited according to Kato and Launder [16]. For the hybrid methods, laminarturbulent transition was taken into account by the  $\gamma$ -model [17], which was previously explored in hybrid RANS-LESmethods by Möller et al. [18] and Möller et al. [19]. The steady RANS methods utilized the  $\gamma$ -Re $_{\theta}$ -model [20] with correlations from Menter et al. [21]. The IDDES method implemented in TRACE was proposed by Shur et al. [22]. The hybrid approaches differ from a pure RANS turbulence model by altering the length scale in the destruction term of the modeled turbulent kinetic energy k. The IDDES length scale  $l_{\text{IDDES}}$  is given as

$$l_{\text{IDDES}} = \tilde{f}_{\text{d}} \left( 1 + f_{\text{e}} \right) l_{\text{RANS}} + \left( 1 - \tilde{f}_{\text{d}} \right) l_{\text{LES}}, \tag{1}$$

in which  $\tilde{f}_{\rm d}$  is the shielding function,  $f_{\rm e}$  the elevating function,  $l_{\rm RANS}$  the RANS length scale, and  $l_{\rm LES}$  the LES length scale. The functions are responsible for weighting the RANS and LES length scale and their respective definition depends on the flow field and the wall distance [22]. The RANS length scale is defined as

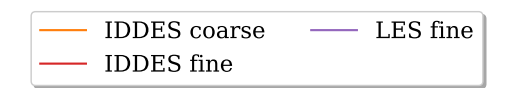
$$l_{\text{RANS}} = \frac{\sqrt{k}}{C_{\mu}\omega} \tag{2}$$

with  $\omega$  being the RANS model's transport variable of specific turbulent dissipation rate.  $C_{\mu}$  is a constant equal to 0.09. The LES length scale is calculated from

$$l_{\rm LES} = C_{\rm DES} \Delta_{\rm IDDES}, \tag{3}$$

in which  $C_{\rm DES}=0.65$ .  $\Delta_{\rm IDDES}$  is the IDDES model's filter width. A vorticity-based subgrid length scale approach according to Shur et al. [23] was chosen. For further explanation about the subfunctions involved in IDDES, we refer to Shur et al. [22] and Gritskevich et al. [24].

The inflow state is prescribed by a 2D inflow profile with end-wall boundary layers. In the midspan, the inlet total pressure of  $p_t = 11644.4\,\mathrm{Pa}$ , the inlet total temperature of  $T_t = 303.25\,\mathrm{K}$ , and the inflow angle of  $\alpha = 41\,^\circ$  (in pitch-wise direction) are prescribed. At the outlet, a flux averaged static pressure of  $p_2 = 9120\,\mathrm{Pa}$  is used. For the turbulence resolving computations, inflow turbulence is generated with a synthetic turbulence generator proposed by Shur et al. [25], which was implemented by Morsbach and Franke [26] and investigated by Matha et al. [27]. In Fig. 2 the decay of turbulence intensity is depicted for the turbulence resolving methods of the different grids on one mid-passage streamline. Between the coarse and fine grid, and the various turbulence treatments the differences in Tu are seen to be negligible. The unphysically high value in Tu for  $x/l_{\rm ax} < -2.1$  can most likely be



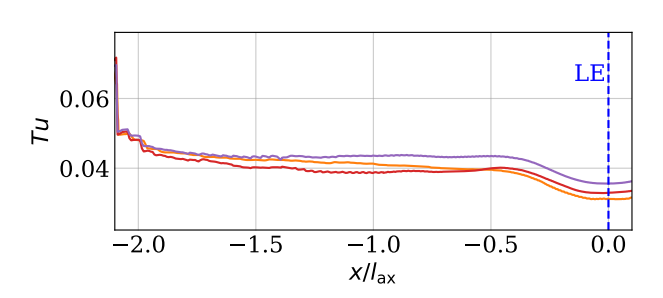


Figure 2: Decay of turbulence intensity derived from resolved turbulent kinetic energy on one midspan streamline

attributed to interpolation errors at the inlet of the domain. At  $x/l_{\rm ax} = -2$ , the turbulence intensity is virtually the same for all grids. The turbulence inflow conditions of the RANS solution are altered to fit the design point and resemble the results from the literature.

To identify the initial transient and quantify the sampling uncertainty, the procedure shown by Bergmann et al. [28] was used. In the following numerical results, in which unsteady data was probed, the 95% confidence interval of the uncertainty is shown. Non-dimensionalization was performed using the boundary layer thickness  $\delta$  calculated on the fine grid with the LES turbulence treatment by calculating the position at which 95% of the free stream total pressure is present.

#### 4 Results

#### 4.1 Evaluation of grid resolution from RANS solution

There are various quality criteria for the spatial resolution of the computational domain of scale resolving simulations, of which some could be analyzed before the turbulence resolving simulation. In Fig. 3 a) the viscous wall units in the midspan and in Fig. 3 b) pitch-wise averaged at the end-wall are shown with  $\Delta I^+$ ,  $\Delta J^+$  and  $\Delta K^+$  referring to the streamwise, the blade normal and the spanwise grid coordinates, respectively. The maximum and averaged values are listed in Tab. 2. Comparing the viscous wall units with Tyacke and Tucker [29] and Georgiadis et al. [30] shows that the coarse, as well as the fine grid are well inside the recommended range for hybrid RANS-LES computations. The fine grid can be seen to be on the edge to qualify for LES-resolution, except in spanwise

direction, in which the value is approximately 3 to 4 times higher than proposed. Rosenzweig et al. [31] even state, that a spanwise resolution of DNS quality ( $\Delta K^+$ <15) is necessary to converge the skin friction coefficient on LPT's suction side. In their presented case, the skin friction coefficient deviates locally by about  $3 \cdot 10^{-4}$  for  $\Delta K^+ < 15$  from the numerical simulations of even higher spanwise resolution. In order to reach a comparable resolution in this study, the number of grid cells would need to be increased by the factor 8. The attempt of a LES-computations on this grid can, therefore, be seen to be rather optimistic. We further need to highlight the fact, that the calculated wall shear stresses of RANS and LES can differ from each other as the flow field is predicted differently. In this case this can be seen in the aft region of the suction side. Here, RANS and LES do not agree in predicting the wall shear stresses due to differences in the prediction of the separation. However, the fundamental prediction of the maximum viscous wall units is generally unaffected, though the position of certain features is influenced.

A way to assess the grid resolution inside the domain on the basis of the RANS solution is to compute the RANS-length scale (s. Eq. 2). Among others, Addat et al. [32], Van Maele et al. [33], and Gant [34] then relate the length scale to the maximum cell dimension  $\Delta$ . Ratios larger 12 indicate that more than 80% of the turbulent kinetic energy are resolved ([33]). In Fig. 4, this ratio is shown for the RANS computation of the coarse and the fine grid in the blade's midspan region. Areas colored red indicate that an eddy of local integral length scale is only discretized by 5 or less grid cells which is generally understood as too poorly resolved. Regions colored blue, however, show a ratio of more than 10 and are therefore seen to be sufficiently well-resolved. According to the ratio, the coarse grid is highly under-resolved for LES. The minimum ratio of 5 is not reached anywhere in the midspan plane. In case of the fine grid, the boundary layer of the blade and the shear layers of the separation show  $l_0/\Delta < 5$  indicating that a low grid resolution is present. In the passage between the blades, a ratio of approximately 7 is apparent, which displays adequate resolution.

In summary, neither of the meshes qualifies for well resolved LES according to the RANS criteria. The length-scale criterion further highlights an insufficient free stream resolution especially in the wake. However, the hybrid methods aim exactly at this deficiency by using RANS modeling of the turbulence in under-resolved regions. For this reason, the prediction accuracy is further assessed.

#### 4.2 Flow field characterization

The flow around the MTU-T161 LPT cascade at Re = 90,000is characterized by a laminar separation bubble on the suction side of the profile. Additionally, passage vortices arise from the interaction of the end-wall boundary layer with the blade's leading edge. The former phenomenon is influenced by Kelvin-Helmholtz instability (s. [5]) and generates anisotropic turbulence (s. [6]) and is, therefore, hard to predict for steady RANS models. In Fig. 5 velocity profiles at midspan of the blade's suction side are shown. Until  $x/l_{\rm ax}=0.5~(10x/l_{\rm ax}=5)$ , each method shows the same at-

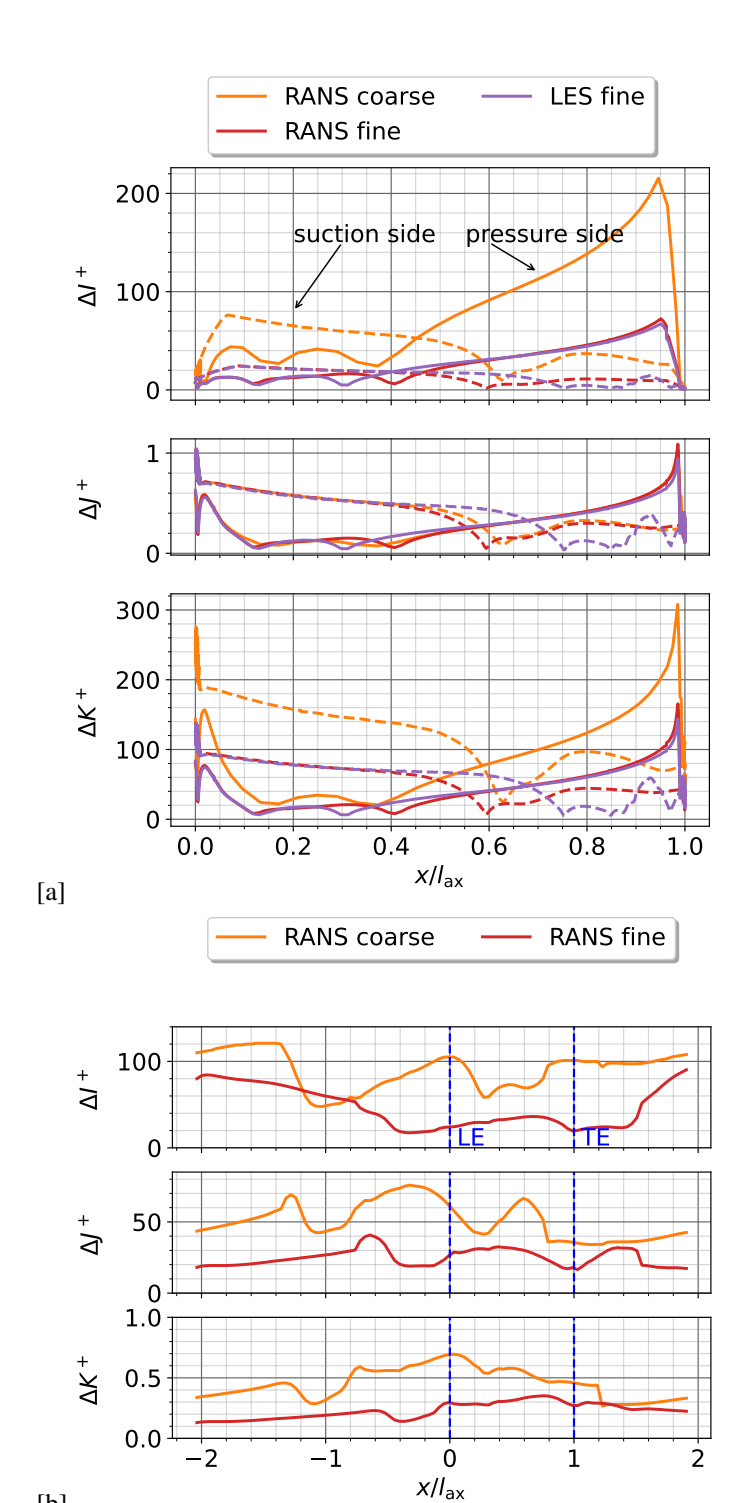


Figure 3: Cell sizes normalized by skin friction and viscosity for the RANS solution of two grid resolutions: a) blade surface at midspan position b) pitch-wise averaged at the endwalls.  $\Delta I^+$  is referring to the global streamwise direction,  $\Delta J^+$ to the direction normal to the blade, and  $\Delta K^+$  to the blade spanwise direction. in a), dashes lines represent the suction side, solid lines represent the pressure side.

[b]

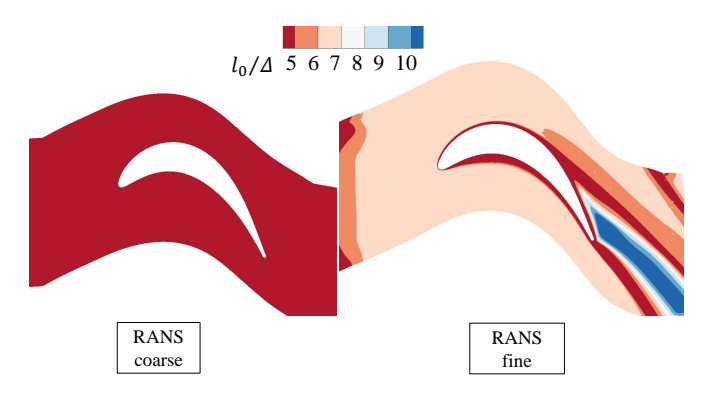


Figure 4: Length scale criterion in the midspan for the coarse and the fine grid. Geometry is distorted.

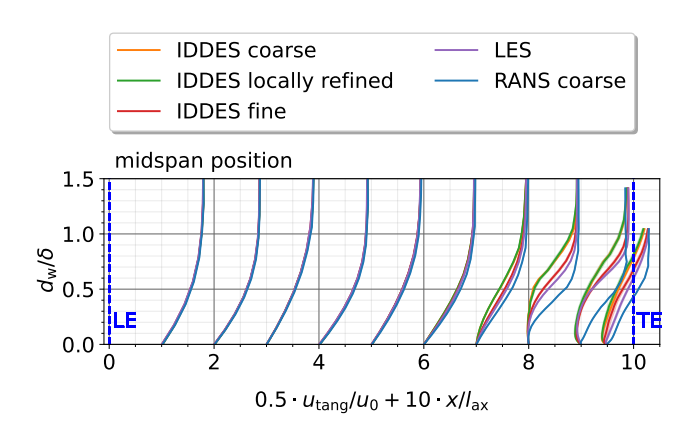


Figure 5: Normalized velocity profiles at midspan shifted by the axial position for various turbulence treatments from leading edge (LE) to trailing edge (TE) of the suction side. The positions of the probes in the computational domain are visualized as blue lines in Fig. 1 a)

tached and laminar velocity profile. At  $x/l_{\rm ax}=0.7$  the steady RANS method shows the initiation of the flow separation, as the velocity gradient at the wall is close to zero. One position downstream a recirculation is predicted by RANS. The turbulence resolving methods show the beginning of flow separation approximately  $0.1~x/l_{\rm ax}$  further downstream and the wall normal extent of the separation bubble is significantly smaller. Downstream of  $x/l_{\rm ax}=0.7$ , the coarse and the locally refined IDDES predict a higher velocity deficit than the fine grid's IDDES and LES, and the RANS method. Smaller differences are visible between the IDDES and the LES on the same fine grid.

To further investigate the flow separation, in Fig. 6 the axial component of the wall shear stress on the suction side of the blade, normalized by an arbitrary reference shear stress is depicted. Upstream of the separation region, the RANS method predicts the highest and the IDDES on the coarse and locally refined grid the lowest wall shear stresses. This trend was expected, as the velocity profiles of Fig. 5 show the respective deficit/surplus in velocity close to the wall. Equivalently, the wall shear stress for the IDDES on the coarse and locally refined grid fall below zero further upstream than the fine grid's LES and IDDES and the RANS method. At this position, the flow separation initiates. Local increases in wall shear stresses

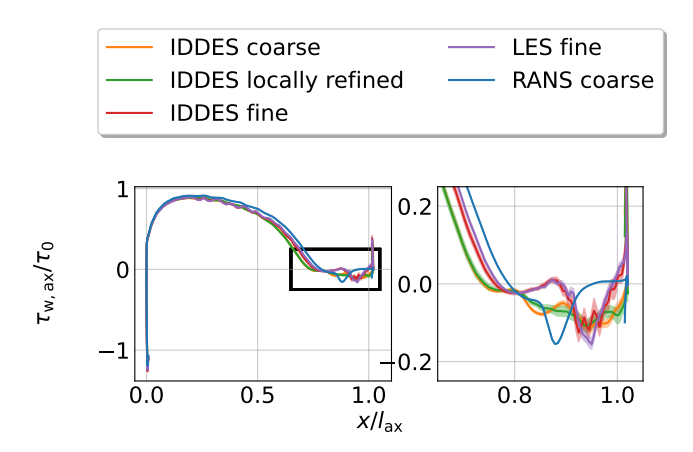


Figure 6: Normalized axial wall shear stress on the suction side of the blade

after the first separation can be a sign of re-energization of the boundary layer due to the local convex deflection of the streamlines. In the case of the IDDES and LES on the fine grid, this even leads to a small area of positive values in  $\tau_{\rm w,ax}$  at  $x/l_{\rm ax}\approx 0.87$  which is a sign of a local reattachment, before a more severe flow separation with a higher velocity recirculation occurs. In total, the separation region is larger for the coarse and locally refined grid than on the fine grid and the LES which directly influences the profile pressure distribution.

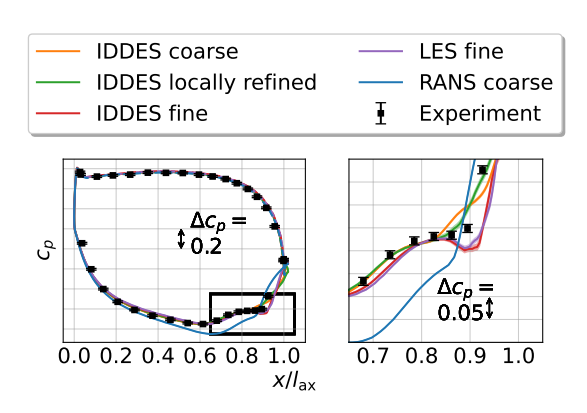


Figure 7: Profile pressure distribution at midspan

In Fig. 7, the profile pressure distribution in the blade's midspan area is shown. All methods show a good agreement with the experiment on the pressure side and in the front region of the suction side of the blade  $(x/l_{\rm ax} < 0.5)$ . In the aft region of the suction side the RANS highly over-predicts the suction peak and shows only a small plateau in  $c_p$ . The turbulence resolving methods agree with each other in predicting the surface pressure more closely. The coarse grid and the locally refined grid show only slight differences, as they rely on the same spatial resolution in this midspan region. The IDDES on the fine grid and the LES result show a good agreement, again relying on the same computational grid. As shown in Fig. 6, the reattachment is being predicted later in case of the fine grids than by the coarser grids, which in general have a better agreement with the experiment in the aft region of the

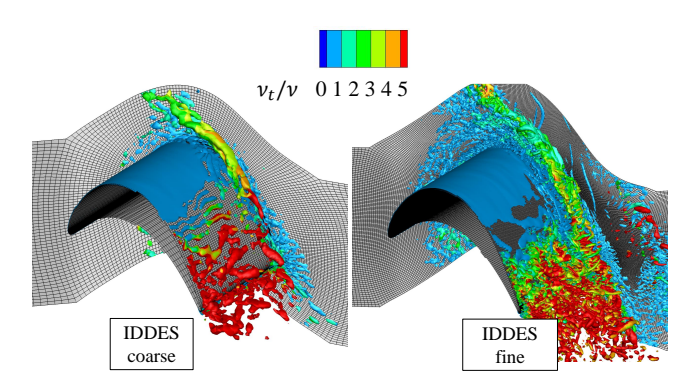


Figure 8: Isovalue of Q-criterion (10<sup>9</sup>) in the aft region of the suction side colored with the ratio of eddy and molecular viscosity for the IDDES model on the coarse and fine grid. Geometry is distorted.

suction side. From this one can conclude that the spatial resolution has only minor influence on the prediction accuracy and that the higher amount of resolved turbulence in IDDES and LES using the fine grid, does not significantly improve the prediction of profile pressure distribution.

In Fig. 8, vortex structures in the blade's aft region are shown in the form of the Q-criterion for IDDES on the fine and the coarse grid. It is visible, that the fine grid is able to resolve finer turbulent structures and a larger variance in scale sizes than the coarse grid. At the end-wall, the structures on the fine grid develop further upstream than on the coarse grid. In both cases, the coloring indicates that a high level of modeled stresses is apparent in the aft region of the blade's suction side.

#### 4.3 Prediction of the end-wall boundary layer

As the end-wall vortex arises from the interaction of the end-wall boundary layer and the blade's leading edge, predicting the upstream boundary layer plays a significant role for the accuracy of the simulation. In Fig. 9, the velocity profiles of the end-wall boundary layer are plotted for the positions A, C, and E (see Fig. 1 for detail), upstream of the cascade inlet plane. The prediction of the turbulence resolving methods and RANS deviate only marginally from each other. The RANS methods show a slightly weaker gradient  $\partial u/\partial d_w$  at the wall, which is especially striking at position C. Consequently, the free stream velocity is slightly higher. The turbulence resolving methods resemble each other for all positions inside the 95% confidence interval of uncertainty. One can conclude, that the prediction of the velocity profile is not altered by the additional turbulence model or the grid refinement.

In Fig. 10, the resolved and the modeled turbulent kinetic energy normalized by an arbitrary reference value  $k_0$  are shown for the scale resolving simulations. Additionally, the ratio of resolved and total turbulent kinetic energy is depicted. At position A the resolved stresses tend to be comparable between all methods and meshes. Further downstream, the LES shows consistently the highest level of resolved stresses. Between the hybrid methods, no significant distinction is possible until position F, where the coarse grid only shows about 30% of the amount of resolved stresses for  $d_{\rm w}/\delta < 0.3$ . One reason for that can be the high amount of  $k_{\rm mod}$  on the coarse

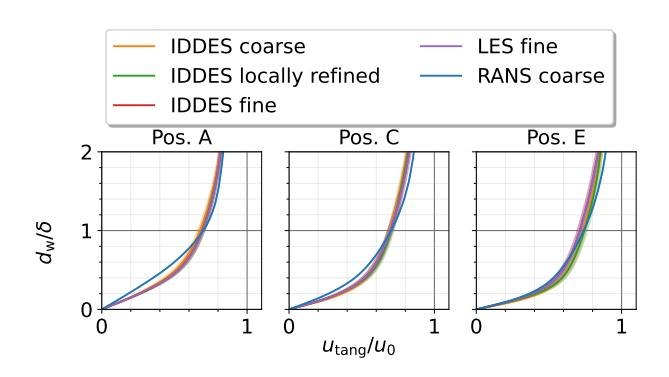


Figure 9: Profiles of tangential velocity in boundary layer cuts of end-wall. Positions of the probes are shown in Fig. 1.

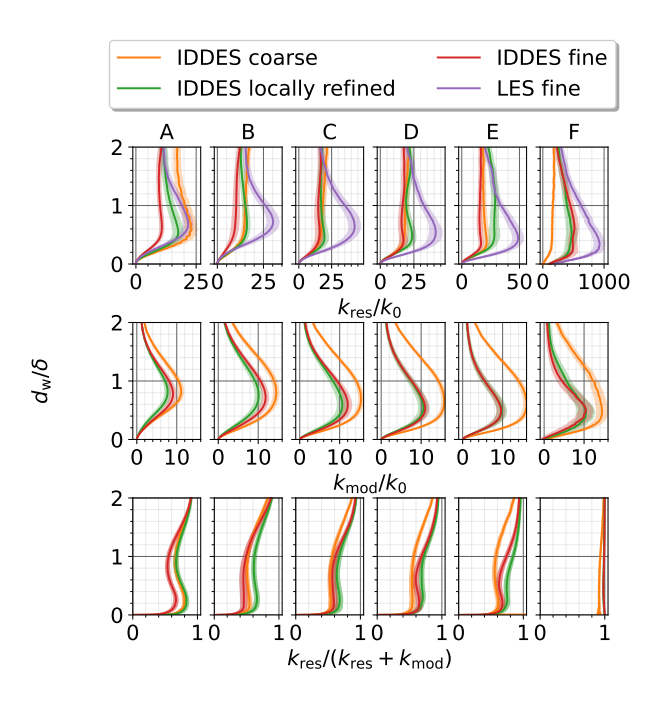


Figure 10: Profiles of normalized modeled and resolved turbulent kinetic energy in boundary layer cuts of end-wall

grid, which dampens fluctuation and, consequently, the formation of turbulence. As a result of the former two quantities, the ratio of resolved to total turbulent kinetic energy is calculated. This ratio is a quality criterion for LES and it is stated by Pope [35] that a threshold of 80% should be reached in pure LES. For an IDDES approaching LES resolution, the criterion should be approached as well. The evaluation confirms that the grid refinement increases the ratio. This is best visible for position E and F. The reason for this is that turbulence requires a specific flow path length to develop.

# 4.4 Flow field analysis and turbulence resolution in the locally refined region

In Fig. 11 the velocity profiles in the refinement region are shown (position in the computational domain is visualized as red lines in Fig. 1 a). Within the first 30% of the blade's axial length, the laminar velocity profiles for each method only exhibit insignificant differences as shown for the midstream region (s. Fig. 5). From that position downstream, the ve-

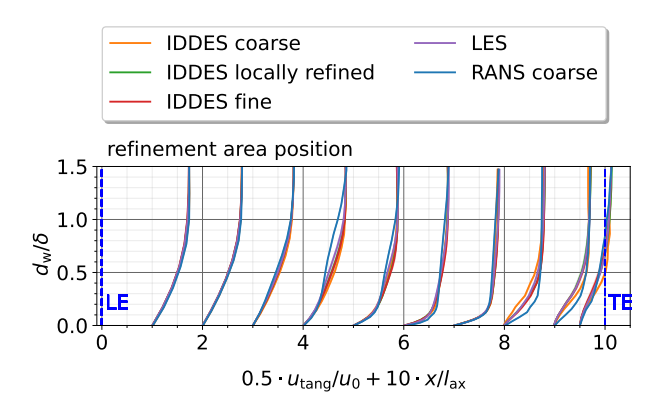


Figure 11: Normalized velocity profiles in refinement region shifted by the axial position from leading edge (LE) to trailing edge (TE) of the suction side. The positions in the computational domain are visualized as red lines in Fig. 1 a).

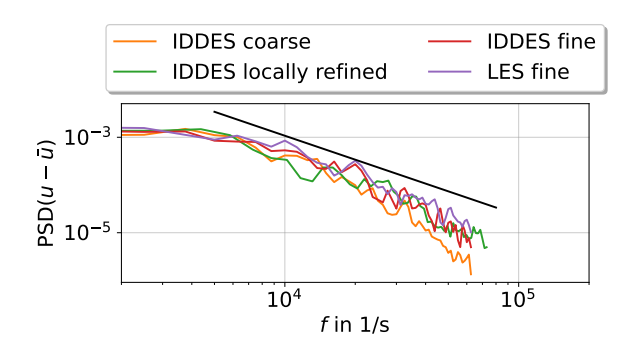


Figure 12: spectral density of the axial velocity fluctuation  $u - \bar{u}$ , with  $\bar{u}$  being the time average velocity component, for the outer most probe of the normal at  $x/l_{\rm ax}$ =0.1 in the refinement region. Black line represents a slope of  $f^{-5/3}$ .

locity profiles of RANS and the turbulence resolving methods deviate from each other. At this spanwise location, no flow separation occurs. Therefore, the prediction in secondary flow features is assumed to be the main reason for differences in the velocity profiles.

In Fig. 12 the power spectral density of the velocity fluctuation in x-direction is presented for all turbulence resolving methods. At the highest frequencies, the coarse grid shows a reduction in the power, which indicates that the highest frequencies, i. e. the small turbulent scales, are not resolved in the same manner as on the finer grids. For  $f = 5 \cdot 10^4$ , the power spectral density of the coarse grid is lower by approximately one order of magnitude. The locally refined grid shows higher frequencies due to a overall slightly higher sampling frequency. This underlines the former observations of resolved stresses and the analytical expectation, that the refinement in IDDES increases the amount of resolved turbulence kinetic energy. It also shows, that even the fine IDDES does not reach the same level of resolved stresses compared to LES on the same mesh, which can be attributed to differences in subgrid scale modelling.

In Fig. 13 the ratio of resolved and total stresses  $(k_{\text{res}}/(k_{\text{res}} + k_{\text{mod}}))$  is shown for the refinement region on an intersection plane with a wall distance of approximately

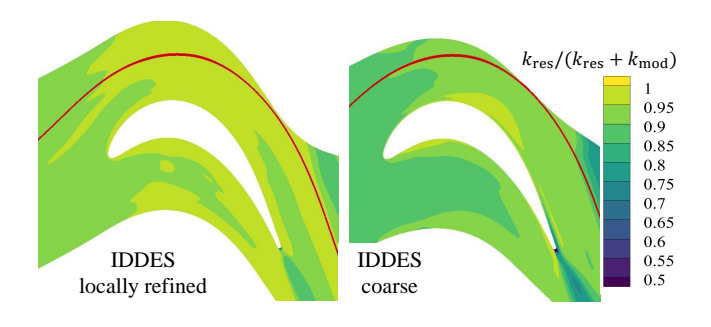


Figure 13: Ratio of resolved and total turbulent kinetic energy in blade-to-blade view at  $z/h \approx -0.46$  in locally refined region of the blade for the different meshes. Geometry is distorted.

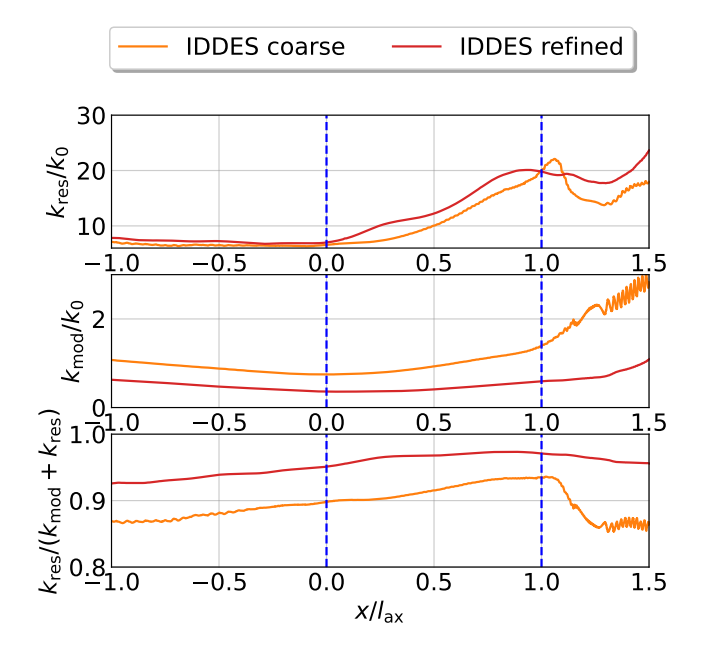


Figure 14: Normalized resolved and modelled turbulent kinetic energy, ratio of resolved and total turbulent kinetic energy for the midpassage streamline shown on Fig. 13

0.04 z/h. In the case of the coarse mesh, an insufficient resolution - in accordance with the 80% guideline - is only visible at the trailing edge with ratios smaller than 0.5. The locally refined grid, however, shows no such deficiencies as the ratio stays consistently above 0.8. The grid refinement, therefore, helps to increase the ratio of resolved and total turbulent kinetic energy. In contrast to the RANS length scale criterion of Fig. 4, the grid resolution in the free stream is evaluated to be adequate, as the coarse and the refined grid as it surpasses the guideline in this area. This is due to a minimal amount of modelled stresses in this area. For a quantitative comparison, the resolved stresses, the modelled stresses and the ratio of the resolved to total stresses is depicted for the colored midpassage streamline in the refinement region in Fig. 14.  $k_{res}$ and  $k_{\text{mod}}$  are here normalized by an arbitrary reference value  $k_0$ . Upstream of the leading edge, the resolved stresses for the locally refined and the coarse grid differ by less than 5% from each other. The grid resolution thereby is not affecting the

decay of turbulence intensity. However, the modelled stresses show a difference of 80 to 100% over the shown streamtrace path. For that reason, the refined grids ratio of resolved to total stresses is higher in the respective positions. According to the ration, both dataset fulfill the guideline in the free stream.

In Fig. 15 the wake loss coefficient, normalized by a constant parameter  $\omega_0$  as  $\omega/\omega_0 = (p_{t,1} - p)/((p_{t,1} - p_2) \cdot \omega_0)$ , is shown for the different numerical solutions and the experiment. Iso-lines represent the experiment in each plot. Two distinct maxima in pressure loss are apparent and can be identified as the vortex pair of passage vortex (PV) and trailing shed vortex (TSV) (s. Rosenzweig et al. [9]). The LES agrees best with the experiment. The position, as well as the amplitude of the pressure loss match the experimental results closely. The fine grid's IDDES solution shows slight deviations from both LES and experiment. The PV is predicted to be too close to the end-wall and the TSV has lower losses in total pressure. Both, the coarse and the locally refined grid show a difference in turning when compared to the LES and IDDES on the fine grid: The pitch-wise position of the wake at midspan deviates by about 0.1y/s towards the pressure side. Inside the locally refined region, the grid matches the contour of the PS more accurately than the coarse grid. Outside of this region, the results resemble each other closely.

Figure 16 shows three distinct cuts at a constant spanwise position in the refinement region. At the position closest to the side-wall (z/h = -0.4375), the LES shows the overall best agreement with the width and the amplitude of the wake, although, the the wake is shifted by approximately 0.05 y/stowards the suction side. The IDDES results predict generally higher losses. The locally refined grid's losses closely resemble the fine grid's ones, while the coarse grid shows the largest deviation from the experiment with an over-prediction of peak loss by about 0.05  $\omega/\omega_0$ . One position further towards the midspan (z/h = -0.375), two observations still hold true: the LES agrees best with the experiment and the locally refined grid's IDDES matches the fine grid's IDDES. The good agreement between the coarse grid and the experiment has to be attributed to cancellation of errors. The over-prediction of losses at z/h = -0.4375 and the underprediction at z/h = -0.3125 could lead to a good agreement in between. Closest to the midspan (z/h = -0.3125) only minor differences between the locally refined grid's IDDES, the fine grid's IDDES, and the LES are visible. All methods under-predict the wake losses by about 0.08  $\omega/\omega_0$  at various positions of the peak's plateau. Besides that, the LES shows a good agreement of the width of the wake and of the losses in the freestream. The same can be said for the locally refined grid, as the prediction of the wake's width lies in between the under-predicting coarse and the over-predicting fine grid for 0.6 < y/s < 0.8.

In Fig. 17, the resolved turbulent kinetic energy  $k_{\rm res}$  of the scale resolving simulations is shown for the same positions in the wake measurement plane downstream of the cascade. Closest to the side-wall (z/h=-0.4375), the IDDES on the coarse grid shows the lowest level of turbulence, underpredicting  $k_{\rm res}$  by about 10  $k_0$  when compared with the locally refined IDDES. The latter dataset generally shows the highest stresses and has a good agreement with the LES at the wake

peak and on the pressure side of the wake (0.4 < y/s < 0.8). One position further towards the midspan, the distinction between the meshes is more pronounced and the curves of resolved stresses closely resemble the wake losses of Fig. 16. The locally refined grid predicts approximately 70% more turbulent kinetic energy than the coarse grid at the peak of the wake, exaggerating the differences in wake losses. The resolved stresses on the locally refined grid are comparable to the stresses on the fine grid. The same analysis holds true for the position closest to the midspan, in which the prediction of the wake's width generally dictates the distribution of resolved stresses.

#### 4.5 Computational Resources

To quantify if the use of a computational method is economically rational, not only the prediction accuracy is of importance, but also computational resources play a significant role. This is why an evaluation on the resources required to obtain a solution has been conducted. An unsteady simulation time of  $5t_c$  for reaching the initial transient and  $15t_c$  for the averaging of statistics was chosen. The steady RANS method shows convergence after 2500 iterations. In order to guarantee a fair comparison, all simulations have been conducted on the exact same set of CPU's running exclusively. For an overview of the resources spent, see Tab. 3 in the appendix. As mentioned in subsection 3.2, a different time-step size needs to be applied for the meshes of different resolution due to the explicit scheme's stability criterion. When looking at IDDES, due to this limitation the fine grid needs a total of 166% and the locally refined grid 200% of the number of time-steps calculated on the coarse grid. The latter might be a consequence of the additional instability arising from the interface between the two mesh resolutions. Moreover, the additional number in grid cells increases the computational cost further. The computation of the locally refined grid is, therefore, about 8.6 times as costly as the computation of the coarse grid. The fine grid is about 15.6 times more expensive, while only a factor of approximately 10 separates the number of grid cells between the two meshes, showing a nonlinear correlation.

Additionally, the cost of the respective turbulence treatment can be highlighted. While LES and IDDES on the fine grid use the same time-step size, the overall computational cost is two times higher for the IDDES approach. This can be due to the three additional transport equations of turbulence and transition modelling which have to be solved during the solution of the hybrid method, as LES does not need to transport the variables k,  $\omega$  and  $\gamma$ . As a consequence, the LES on the fine grid was as computationally expensive as the IDDES on the locally refined grid, which has only 42% of the number of grid cells. From that perspective, the benefit of IDDES for this test case is questionable and only the use of IDDES on the coarse mesh can be recommended.

## 5 Conclusion

We evaluated the effects of local mesh refinements on the prediction accuracy of IDDES for its application in turbomachinery. A mesh refinement strategy, which focuses on the reso-

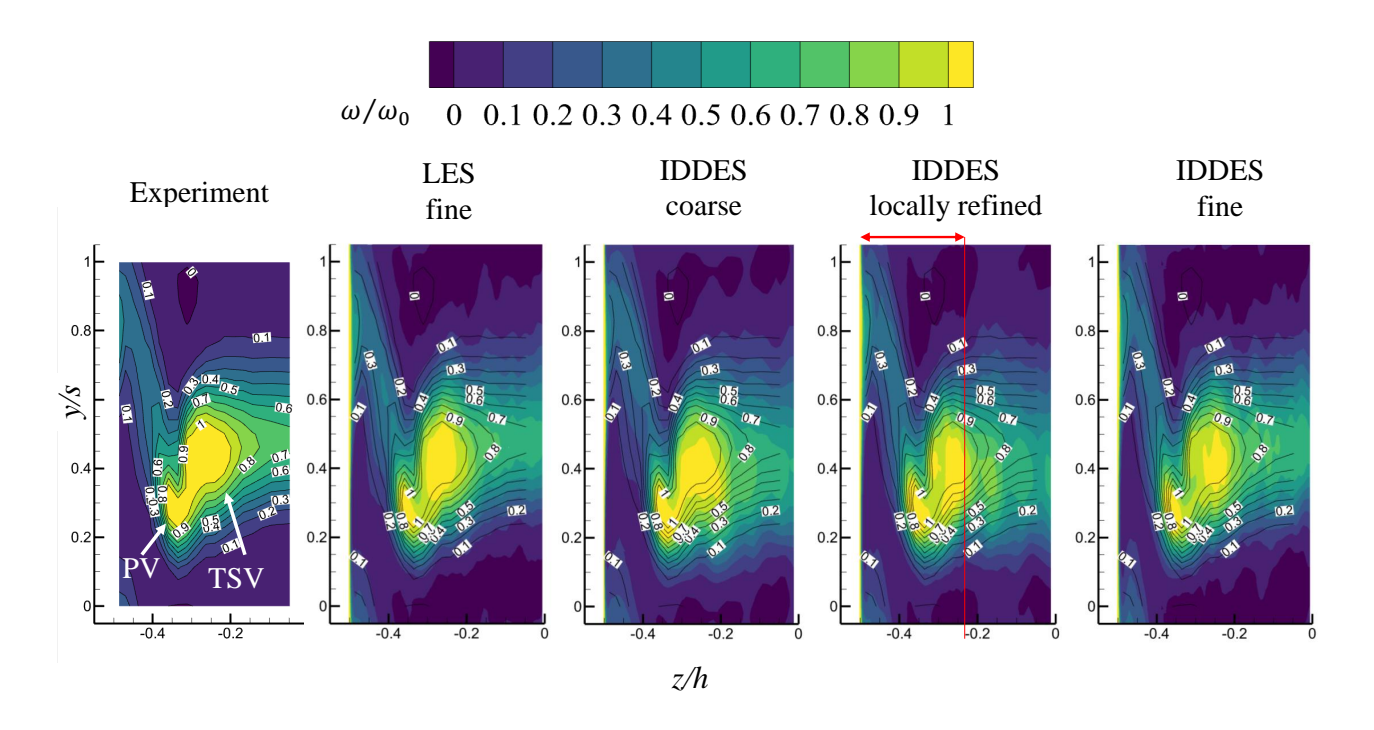


Figure 15: Wake losses at  $x/l_{\rm ax} = 1.4$ . Experimental data for reference is added by line contours. Refinement region is highlighted by a red arrow.

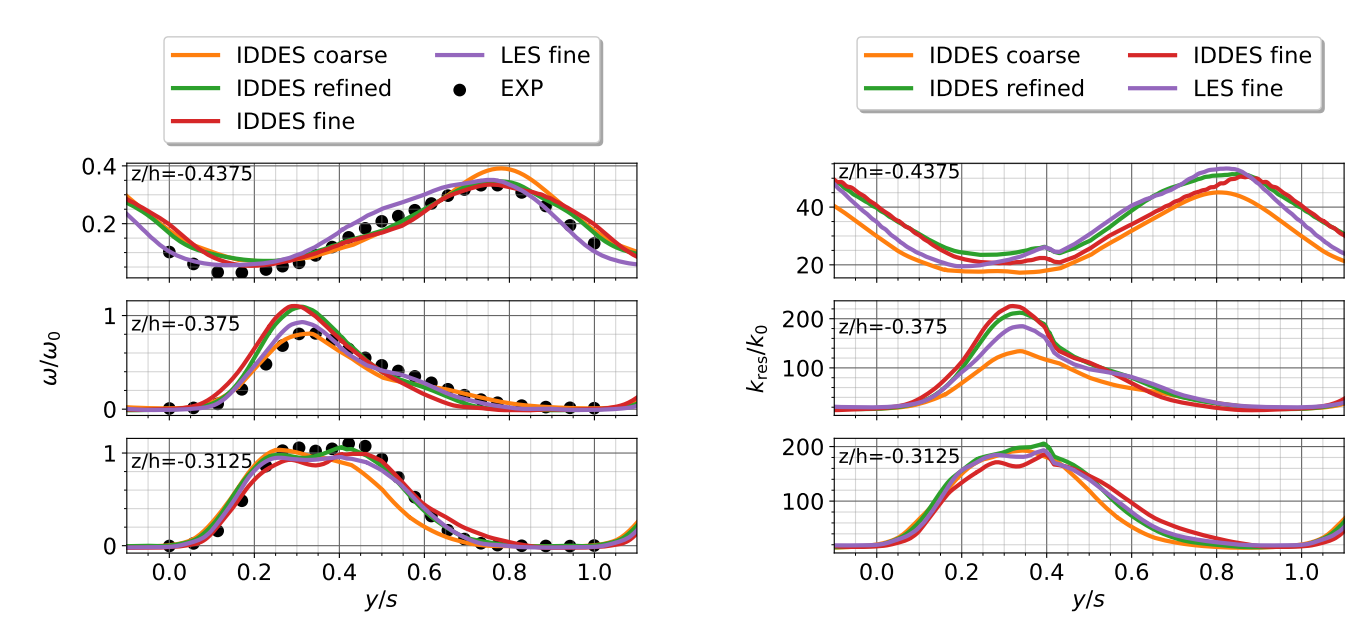


Figure 16: Normalized wake loss coefficient for different spanwise positions at  $x/l_{\rm ax}=1.4$ .

Figure 17: Normalized resolved turbulent kinetic energy in the wake for different spanwise positions at  $x/l_{\rm ax}=1.4$ .

lution of the interaction of the end-wall boundary layer with the leading edge of the MTU-T161 low-pressure turbine has been introduced. In the assessment of the predicted flow field, the solution of the locally refined mesh has been compared to homogeneously coarse and fine meshes with the same turbulence model, as well as RANS and LES computations. The study focused at first on predicting the end-wall boundary layer and on the locally refined flow field at the blade. In the last section, the computational expenses for the different methods have been evaluated. The main conclusions are:

- The local mesh refinement leads to a decrease in modeled turbulence and to an increase in resolved stresses. For the end-wall boundary layer, it was shown that the ratio of resolved to total turbulent kinetic energy is increased in the boundary layer of wall bound flows, leading to a well-resolved boundary layer. Benefits for the prediction of velocity profiles in the end-wall boundary layer were found to be marginal.
- The prediction of wake losses dominated by the secondary flow was improved by the mesh refinement. The fine grid and the locally refined show virtually the same prediction in the refinement region. However, the prediction lacks in accuracy in regions further away from the locally refined end-wall. This deficiency is expected with the RANS-style grid at the blade's midspan.
- The use of the turbulence resolving hybrid method on the coarse grid was able to outperform the steady RANS solution but shows significant deficiencies when compared to the fine mesh irrespective of the turbulence's treatment.
- Evaluating the computational resources showed that a
  possible time-step limitation due to grid refinements has
  a high impact on the overall cost of the simulations. Grid
  interfaces require a further reduction in time-step size for
  retaining stability. The computational cost of additional
  turbulence and transition models was found to be a significant factor to consider, when choosing between hybrid and LES computations of high grid resolution.

In summary, the test case presented an opportunity to alter the solution accuracy of hybrid methods locally. Evaluating the computational resources showed that the method was not cost effective as it increased the required number of timesteps by a factor of 2. LES on a moderately fine mesh is able to provide a prediction closer to the experiment and comes in this unfavorable case with the same computational cost. Given the combination of the factors mentioned, the authors do not believe this approach has the potential to become competitive for the class of flows presented. However, the approach would benefit from unstructured grids with a smooth transition between coarse regions and local refinements and higher Reynolds number flows. Future work should, therefore, focus more on problems of industrial perspective, or deal with ways to decouple the time-step between different flow field regions as achievable in zonal hybrid RANS-LES.

## Acknowledgments

The authors gratefully acknowledge the computing time made available to them on the high-performance computer "Lise" at the NHR Center NHR@ZIB. This center is jointly supported by the Federal Ministry of Education and Research and the state governments participating in the NHR (www.nhrverein.de/unsere-partner). The authors gratefully thank the Leibniz Universität Hannover (LUIS) for providing computational resources. We acknowledge the contribution of the DLR Institute of Propulsion Technology and MTU Aero Engines AG for facilitating TRACE.

Nomenclature		Superscripts			
		0	reference/normalization constant		
c	velocity in m/s				
h	spanwise extend of the cascade in m	ax	axial		
_		С	convective		
I	streamwise grid coordinate	mod	modeled		
J	blade-normal grid	res	resolved		
	coordinate	SLS	subgrid length		
K	spanwise grid co- ordinate				
	ordinate	t	turbulent		
k	turbulent kinetic energy in $m^2/s^2$	tan	tangential		
l	length scale in m	tot	total		
p	pressure in Pa	W	wall		
S	pitch of the cas-	Acronyms			
	cade in m	CFD	computational		
t	time in s		fluid dynamics		
x	axial coordinate in m	IDDES	improved delayed eddy simulation		
у	pitchwise coordi- nate in m	LE	leading edge		
z	spanwise coordi- nate in m	LES	large eddy simula- tion		
Greek	symbols	PV	passage vortex		
Δ	filter width in m	RANS	Reynolds averaged Navier-Stokes		
δ	boundary layer thickness in m		(equations)		
ω	pressure loss coef-	TE	tailing edge		
30	ficient	TSV	trailing shed vortex		

### References

[1] J. Voigt, H. Seehausen, F. M. Möller, and L. Wein. "Forcing LES in Seamless Hybrid RANS-LES Meth-

- odsby Local Mesh Refinement". In: *Proceedings of the International Gas Turbine Congress* 2023, *IGTC*-2023-093.
- [2] T. Kořínek, K. Fraňa, J. Hujer, and J. Škarohlíd. "Influence of local grid refinement on prediction of impinging jet heat transfer using Scale-Resolving-Simulation methods". In: *Case Studies in Thermal Engineering* 36 (2022), p. 102159. DOI: https://doi.org/10.1016/j.csite.2022.102159.
- [3] A. ElCheikh and M. ElKhoury. "Effect of local grid refinement on performance of scale-resolving models for simulation of complex external flows". In: *Aerospace* 6.8 (2019), p. 86. DOI: https://doi.org/10.3390/aerospace6080086.
- [4] R. Entlesberger, M. Martinstetter, and W. Staudacher. "Untersuchungen am Turbinengitter T161 zur Bestimmung der Profildruckverteilung und der Gittercharakteristik". In: *Institutsbericht LRT-WE12-05/12. Universität der Bundeswehr München.* (2005).
- [5] C. Müller-Schindewolffs, R.-D. Baier, J. R. Seume, and F. Herbst. "Direct Numerical Simulation Based Analysis of RANS Predictions of a Low-Pressure Turbine Cascade". In: *Journal of Turbomachinery* 139.8 (Mar. 2017), p. 081006. ISSN: 0889-504X. DOI: 10.1115/ 1.4035834.
- [6] N. Fard Afshar, D. Kozulovic, S. Henninger, J. Deutsch, and P. Bechlars. "Turbulence anisotropy analysis at the middle section of a highly loaded 3D linear turbine cascade using Large Eddy Simulation". In: *Journal of the Global Power and Propulsion Society* 7 (2023), pp. 71–84. DOI: 10.33737/jgpps/159784.
- [7] C. Morsbach, M. Bergmann, A. Tosun, B. F. Klose, E. Kügeler, and M. Franke. "Large eddy simulation of a low-pressure turbine cascade with turbulent end wall boundary layers". In: *Flow Turbulence Combust* (2023). DOI: 10.1007/s10494-023-00502-6.
- [8] M. Rosenzweig, M. Kozul, R. Sandberg, M. Marconcini, and R. Pacciani. "High-Fidelity Simulations and RANS Analysis of a Low-Pressure Turbine Cascade in a Spanwise-Diverging Gas Path-End-Wall Flow Analysis and Loss Generation Mechanisms". In: *Turbo Expo: Power for Land, Sea, and Air.* Vol. 87097. American Society of Mechanical Engineers. 2023, V13BT30A003.
- [9] M. Rosenzweig, M. Kozul, and R. D. Sandberg. "Unsteady Loss Mechanisms in Low-Pressure Turbines With Diverging End-Walls Studied via High-Fidelity Simulation". In: *Turbo Expo: Power for Land, Sea, and Air*. Vol. 125408. American Society of Mechanical Engineers. 2024.
- [10] G. Geiser, J. Wellner, E. Kügeler, A. Weber, and A. Moors. "On the Simulation and Spectral Analysis of Unsteady Turbulence and Transition Effects in a Multistage Low Pressure Turbine". In: *Journal of Turbomachinery* (2019). DOI: 10.1115/1.4041820.

- [11] P. Roe. "Approximate Riemann Solvers, Parameter Vectors, and Difference Schemes". In: *Journal of Computational Physics* 43.2 (1981), pp. 357–372.
- [12] B. Van Leer. "Towards the ultimate conservative difference scheme. V. A second-order sequel to Godunov's method". In: *Journal of computational Physics* 32.1 (1979), pp. 101–136. DOI: 10.1016/0021-9991(79) 90145-1.
- [13] A. Travin, M. Shur, M. Strelets, and P. Spalart. "Physical and numerical upgrades in the detached-eddy simulation of complex turbulent flows". In: *Advances in LES of Complex Flows: Proceedings of the Euromech Colloquium 412, held in Munich, Germany 4–6 October 2000.* Springer. 2002, pp. 239–254. DOI: 10.1007/0-306-48383-1\_16.
- [14] F. Nicoud and F. Ducros. "Subgrid-Scale Stress Modelling Based on the Square of the Velocity Gradient Tensor". In: *Flow Turbulence and Combustion* 62 (Sept. 1999), pp. 183–200. DOI: 10 . 1023 / A: 1009995426001.
- [15] F. R. Menter, M. Kuntz, R. Langtry, et al. "Ten years of industrial experience with the SST turbulence model". In: *Turbulence, heat and mass transfer* 4.1 (2003), pp. 625–632.
- [16] K. Kato. "The modeling of turbulent flow around stationary and vibrating square cylinders". In: *Proc. of 9th Symp. Turbulent Shear Flows.* 1993, pp. 1041–1046.
- [17] F. R. Menter, P. E. Smirnov, T. Liu, and R. Avancha. "A One-Equation Local Correlation-Based Transition Model". In: *Flow, Turbulence and Combustion* 335 (2015). DOI: 10.1007/s10494-015-9622-4.
- [18] F. M. Möller, P. G. Tucker, Z.-N. Wang, C. Morsbach, and M. Bergmann. "On the Prediction of Separation-Induced Transition by Coupling Delayed Detached-Eddy Simulation with γ-Transition Model". In: 15th European Conference on Turbomachinery Fluid dynamics & Thermodynamics. ETC, Apr. 2023. DOI: 10. 29008/ETC2023-375.
- [19] F. M. Möller, P. G. Tucker, Z.-N. Wang, and C. Morsbach. "Transitional Delayed Detached-Eddy Simulation for a Compressor Cascade: A Critical Assessment". In: *Journal of Propulsion and Power* 40.4 (2024), pp. 533–546. DOI: 10.2514/1.B39344.
- [20] R. B. Langtry and F. R. Menter. "Correlation-based transition modeling for unstructured parallelized computational fluid dynamics codes". In: AIAA journal 47.12 (2009), pp. 2894–2906. DOI: 10.2514 / 1.42362.
- [21] F. R. Menter, R. B. Langtry, S. Likki, Y. Suzen, P. Huang, and S. Völker. "A correlation-based transition model using local variables—part I: model formulation". In: *Journal of turbomachinery* 128.3 (2006), pp. 413–422. DOI: 10.1115/1.2184352.

- [22] M. Shur, P. Spalart, M. Strelets, and A. Travin. "A hybrid RANS-LES approach with delayed-DES and wall-modelled LES capabilities". In: *International Journal of Heat and Fluid Flow* 29 (Dec. 2008), pp. 1638–1649. DOI: 10.1016/j.ijheatfluidflow.2008.07.001.
- [23] M. L. Shur, P. R. Spalart, M. K. Strelets, and A. K. Travin. "An enhanced version of DES with rapid transition from RANS to LES in separated flows". In: *Flow, turbulence and combustion* 95 (2015), pp. 709–737. DOI: 10.1007/s10494-015-9618-0.
- [24] M. S. Gritskevich, A. V. Garbaruk, J. Schütze, and F. R. Menter. "Development of DDES and IDDES formulations for the k-ω shear stress transport model". In: *Flow, turbulence and combustion* 88.3 (2012), pp. 431–449. DOI: 10.1007/s10494-011-9378-4.
- [25] M. Shur, P. Spalart, M. Strelets, and A. Travin. "Synthetic Turbulence Generators for RANS-LES Interfaces in Zonal Simulations of Aerodynamic and Aeroacoustic Problems". In: *Flow Turbulence and Combustion* 93 (June 2014), pp. 63–92. DOI: 10.1007/s10494-014-9534-8.
- [26] C. Morsbach and M. Franke. "Analysis of a synthetic turbulence generation method for periodic configurations". In: *ERCOFTAC Workshop Direct and Large-Eddy Simulation 11* (2017). DOI: 10.1007/978-3-030-04915-7\_23.
- [27] M. Matha, C. Morsbach, and M. Bergmann. "A comparison of methods for introducing synthetic turbulence". In: 7th European Conference on Computational Fluid Dynamics (2018).
- [28] M. Bergmann, C. Morsbach, G. Ashcroft, and E. Kügeler. "Statistical Error Estimation Methods for Engineering-Relevant Quantities From Scale-Resolving Simulations". In: *Journal of Turbomachinery* 144.3 (Oct. 2021). ISSN: 0889-504X. DOI: 10.1115/1.4052402.
- [29] J. C. Tyacke and P. G. Tucker. "Future Use of Large Eddy Simulation in Aero-Engines". In: *ASME Journal of Turbomachinery* 137.8 (Aug. 2015). 081005. ISSN: 0889-504X. DOI: 10.1115/1.4029363.
- [30] N. J. Georgiadis, D. P. Rizzetta, and C. Fureby. "Large-eddy simulation: current capabilities, recommended practices, and future research". In: *AIAA journal* 48.8 (2010), pp. 1772–1784. DOI: 10.2514/1.J050232.
- [31] M. Rosenzweig, S. Giaccherini, L. Pinelli, M. Kozul, R. Sandberg, M. Marconcini, and R. Pacciani. "Best-Practice Guidelines for High-Fidelity Simulations Based on Detailed Analysis of a Highly-Loaded Low-Pressure Turbine Cascade". In: *Turbo Expo: Power for Land, Sea, and Air.* Vol. 87097. American Society of Mechanical Engineers. 2023, V13BT30A021. DOI: https://doi.org/10.1115/GT2023-102697.

- [32] Y. Addad, S. Benhamadouche, and D. Laurence. "The negatively buoyant wall-jet: LES results". In: *International journal of heat and fluid flow* 25.5 (2004), pp. 795–808. DOI: https://doi.org/10.1016/j.ijheatfluidflow.2004.05.008.
- [33] K. Van Maele and B. Merci. "Application of RANS and LES field simulations to predict the critical ventilation velocity in longitudinally ventilated horizontal tunnels". In: Fire Safety Journal 43.8 (2008), pp. 598–609. ISSN: 0379-7112. DOI: https://doi.org/10.1016/j.firesaf.2008.02.002.
- [34] S. Gant. "Practical Quality Measures for Large-Eddy Simulation". In: 13 (Jan. 2010). DOI: 10.1007/978-90-481-3652-0\_33.
- [35] S. B. Pope. "Ten questions concerning the large-eddy simulation of turbulent flows". In: *New journal of Physics* 6.1 (2004), p. 35. DOI: 10.1088/1367-2630/6/1/035.

Table 2: Details about the wall-coordinates of the different grids at midspan and pitch-wise averaged at the end-wall

grid	position	$\max \Delta I^+, \overline{\Delta I^+}$	$\max \Delta J^+, \overline{\Delta J^+}$	$\max \Delta K^+, \overline{\Delta K^+}$
coarse	midspan - suction side	76, 31	1.04, 0.45	275, 126
coarse	midspan - pressure side	215, 50	1.01, 0.41	308, 116
fine	midspan - suction side	24, 11.5	1.04, 0.41	137, 58
fine	midspan - pressure side	72, 23	1.08, 0.37	165, 53
coarse	end-wall - pitch-wise averaged	121, 91	75.8, 50.9	0.695, 0.456
fine	end-wall - pitch-wise averaged	90.3, 46.66	40.8, 24.9	0.352, 0.229

Table 3: Details about the numerical grids, time discretization and averaging times for each numerical method

modeling method	RANS		IDDES			LES
grid name	coarse	fine	coarse	locally refined	fine	fine
number of grid cells in 10 <sup>6</sup>	1.9	20.6	1.9	8.6	20.6	
time-step size in $10^{-8}$ s	/	/	3.333	1.66	2	2
time-steps per $t_c$ in $10^3$	/	/	23	46	39	39
used CPU hours per t <sub>c</sub>	/	/	383	3306	5980	3098
used CPU hours for solution	18	350	7664	66122	119600	61962